UNIVERSITY OF COPENHAGEN

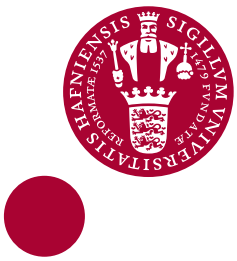

Monitoring CO2 migration in a shallow sand aquifer using 3D crosshole electrical resistivity tomography

Yang, Xianjin ; Lassen, Rune Nørbæk; Jensen, Karsten Høgh; Zibar, Majken Caroline Looms

Published in:
International Journal of Greenhouse Gas Control

DOI:
10.1016/j.ijggc.2015.09.005

Publication date:
2015

Document version
Publisher's PDF, also known as Version of record

Citation for published version (APA):
Yang, X., Lassen, R. N., Jensen, K. H., & Zibar, M. C. L. (2015). Monitoring CO2 migration in a shallow sand aquifer using 3D crosshole electrical resistivity tomography. *International Journal of Greenhouse Gas Control*, *42*, 534–544. https://doi.org/10.1016/j.ijggc.2015.09.005

Download date: 08. apr.. 2020

International Journal of Greenhouse Gas Control 42 (2015) 534–544

Contents lists available at ScienceDirect

International Journal of Greenhouse Gas Control

journal homepage: www.elsevier.com/locate/ijggc

Monitoring CO_2 migration in a shallow sand aquifer using 3D crosshole electrical resistivity tomography

Xianjin Yang[a,*], Rune N. Lassen[b], Karsten H. Jensen[b], Majken C. Looms[b]

[a] Lawrence Livermore National Laboratory, 7000 East Ave, Livermore, CA 94550, United States
[b] University of Copenhagen, Department of Geosciences and Natural Resource Management, Øster Voldgade 10, DK-1350 Copenhagen, Denmark

ARTICLE INFO

Article history:
Received 11 January 2015
Received in revised form 14 August 2015
Accepted 5 September 2015
Available online 25 September 2015

Keywords:
Monitoring
Electrical resistivity tomography (ERT)
Electrical conductivity (EC)
Dissolved CO_2
Gaseous CO_2
Shallow aquifer
Crosshole

ABSTRACT

Three-dimensional (3D) crosshole electrical resistivity tomography (ERT) was used to monitor a pilot CO_2 injection experiment at Vrøgum, western Denmark. The purpose was to evaluate the effectiveness of the ERT method for detection of small electrical conductivity (EC) changes during the first 2 days of CO_2 injection in a shallow siliciclastic aquifer and to study the early-time behavior of a controlled small gaseous CO_2 release. 45 kg of CO_2 was injected over a 50-h period at 9.85 m depth. ERT data were collected using horizontal bipole-bipole (HBB) and vertical bipole-bipole (VBB) arrays. The combined HBB and VBB data sets were inverted using a difference inversion algorithm for cancellation of coherent noises and enhanced resolution of small changes. ERT detected the small bulk EC changes (<10%) from conductive dissolved CO_2 and resistive gaseous CO_2. The primary factors that control the migration of a CO_2 plume consist of buoyancy of gaseous CO_2, local heterogeneity, groundwater flow and external pressure exerted by the injector. The CO_2 plume at the Vrøgum site migrated mostly upward due to buoyancy and it also skewed toward northeastern region by overcoming local groundwater flow. The conductive eastern part is more porous and becomes the preferential pathway for the CO_2 plume, which was trapped within the slightly more porous glacial sand layer between 5 m and 10 m depths. The gaseous and dissolved CO_2 plumes are collocated and grow in tandem for the first 24 h and their opposite effects resulted in a small bulk EC increase. After raising the injection rate from 10 g/min to 20 g/min at the 24-h mark, the CO_2 plume grew quickly. The bulk EC changes from ERT agreed partially with water sample EC and GPR data. The apparent disagreement between high CO_2 gas saturation and prevailing positive bulk EC changes may be caused by limited and variable ERT resolution, low ERT sensitivity to resistive anomalies and uncalibrated CO_2 gas saturation. ERT data show a broader CO_2 plume while water sample EC had higher fine-scale variability. Our ERT electrode configuration can be optimized for more efficient data acquisition and better spatial resolution.

© 2015 The Authors. Published by Elsevier Ltd. This is an open access article under the CC BY license (http://creativecommons.org/licenses/by/4.0/).

1. Introduction

A primary risk with geological carbon sequestration is the leakage of CO_2 into a fresh groundwater aquifer from a deep storage. Injection-induced fluid pressure gradient may push brine and CO_2 out of a deep storage formation through potential leakage pathways such as a fault or an abandoned well. CO_2 may also leak into a shallow aquifer from a deep storage solely by buoyancy forces because the density of supercritical CO_2 is less than that of water or brine. As the CO_2 saturated brine is depressurized, CO_2 exsolves from solution. One impact of CO_2 leakage is the alteration of groundwater quality by the intrusion of trace elements, which increases total dissolved solids (TDS) of groundwater (Lions et al., 2014). Extensive studies have been done recently on the environmental impact of CO_2 leakage on a shallow aquifer (Kharaka et al., 2010; Le Roux et al., 2013; Trautz et al., 2013; Strazisar et al., 2009; Carroll et al., 2014; Denchik et al., 2014). Electrical conductivity (EC) has become a proven and effective indicator for detection of dissolved CO_2 in a vadose zone (Strazisar et al., 2009; Zhou et al., 2012) or in a shallow aquifer (Denchik et al., 2014; Trautz et al., 2013; Lamert et al., 2012; Auken et al., 2014) and for detection of supercritical CO_2 in a deep saline formation (Kiessling et al., 2010; Bergmann et al., 2012; Carrigan et al., 2013).

Gaseous CO_2 is soluble in pore water in a shallow aquifer and its solubility in water is 1.45 g/L at 25 °C and 100 kPa. The geochemical processes following a CO_2 leakage into a shallow aquifer include reduced pH due to the formation of carbonic acid and elevated

* Corresponding author at: P.O. Box 808, L-231, Livermore, CA 94551, United States.
E-mail address: yang25@llnl.gov (X. Yang).

http://dx.doi.org/10.1016/j.ijggc.2015.09.005
1750-5836/© 2015 The Authors. Published by Elsevier Ltd. This is an open access article under the CC BY license (http://creativecommons.org/licenses/by/4.0/).

EC due to dissolved CO_2 and mineral dissolution in the groundwater (Dethlefsen et al., 2013; Cahill and Jakobsen, 2013). The elevated water EC in a shallow aquifer may be detected by water sampling (Trautz et al., 2013), in situ EC measurements (Lamert et al., 2012), surface resistivity imaging (Le Roux et al., 2013; Auken et al., 2014), surface conductivity mapping (Pettinelli et al., 2004), airborne electromagnetic imaging (Costard and Paine, 2015), and crosshole electrical resistivity tomography (Dafflon et al., 2013).

The elevated EC due to dissolved CO_2 in a shallow aquifer is contrary to the effect of free-phase supercritical CO_2 in a deep saline formation where nonconductive supercritical CO_2 displaces conductive brine and produces resistive anomalies (Kiessling et al., 2010; Schmidt-Hattenberger et al., 2013; Carrigan et al., 2013).

Injection of CO_2 gas in a vadose zone had a negligible effect on water saturation (Le Roux et al., 2013). The gaseous CO_2 displaced air but not the conductive pore water. This gas substitution process did not alter the bulk EC of soil. Instead, the observed EC may increase as a result of CO_2 dissolution in the pore fluid. However, rainfall may also increase the bulk EC of soil and complicate data interpretation (Zhou et al., 2012).

Le Roux et al. (2013) investigated CO_2 gas migration in a carbonate vadose zone with 2D time lapse electrical resistivity imaging in Gironde, France. Dissolution of CO_2 in pore water forms dissolved inorganic carbon that includes carbonic acid (H_2CO_3), bicarbonate (HCO_3^-) and carbonate (CO_3^{2-}). These species increased EC of pore water, as well as the bulk EC of soils.

A gaseous CO_2 injection experiment through a horizontal perforated pipe at 2–2.3 m depth was conducted at the ZERT field site in Bozeman, Montana. Kharaka et al. (2010) showed rapid and significant increases in alkalinity (400–1300 mg/l), concentrations of Ca (90–240 mg/l), Mg (25–70 mg/l), Fe (5–1200 ppb) and Mn (5–1400 ppb), and water EC (600–1800 μS/cm) since CO_2 injection began in a shallow aquifer. The maximum 200% increase in water EC was observed 2 weeks following CO_2 injection at an injection rate of 300 kg/day.

Trautz et al. (2013) conducted a field experiment in Escatawpa, Mississippi with a continuous release of groundwater containing dissolved CO_2 for 7 months to study the effect of dissolved CO_2 on a shallow aquifer. The dissolution of CO_2 resulted in a sustained drop of about 3 pH units but alkalinity and EC exhibited a short-term pulse behavior. EC in a nearby monitoring well started to increase 8–10 days after injection began, reached a peak value after 23–24 days and then decreased to the level slightly above the background. This water EC pulse signature agrees with Kharaka et al. (2010) and suggests a fast depletion of metals from their sources at the front of the low pH plume. However, the results may depend on the injection rate and amount of CO_2 dissolved in water.

Combining geoelectrical monitoring and multiphase flow modeling can be a useful approach for understanding of gaseous CO_2 migration in a shallow aquifer (Lamert et al., 2012). Gaseous CO_2 flew upwards relatively fast along a discrete gas channel and a gas pool was formed in a glacial loam layer. A dissolved CO_2 plume grew vertically initially and then laterally. They found variations of apparent EC were in the order of 15–30%.

The increase of pore fluid EC due to CO_2 intrusion in a noncarbonate aquifer is an order of magnitude smaller than that in a carbonate aquifer. The fluid EC in a noncarbonate aquifer rises very slowly in response to CO_2 injection and its change after 24 h is roughly seven times smaller than the maximum value reached in 1 year (Fahrner et al., 2011). In addition, the opposite effects of coexistent gaseous and dissolved CO_2 on the bulk EC tend to cancel each other and lead to very small bulk EC changes. These effects pose a significant challenge on ERT monitoring at the early stage of CO_2 injection.

We noted that there existed many CO_2 injection and EC measurement scenarios to study the impact of CO_2 injection on a shallow groundwater system. One may inject gaseous CO_2 or water containing dissolved CO_2, which may be injected in a carbonate or siliciclastic aquifer or in a vadose zone. Electrical conductivity can be measured by water sampling for water EC, in situ monitoring for local bulk EC or electrical resistivity imaging for bulk EC distribution with either surface or downhole electrodes.

We conducted a pilot CO_2 gas injection experiment in a shallow siliciclastic unconfined aquifer in Vrøgum, western Denmark to simulate a CO_2 leak from a deep storage (Cahill and Jakobsen, 2013; Lassen et al., 2015). The primary goal of this pilot CO_2 injection experiment was to study the site hydrogeological conditions, likely aquifer responses to the injection and performance of the monitoring system and design. The results of this pilot injection would aid a larger-scale experiment initiated on May 14, 2012 at the nearby site (Auken et al., 2014; Cahill et al., 2014; Doetsch et al., 2015). We deployed a 3D crosshole electrical resistivity tomography (ERT) system for tracking CO_2 plume migration and distribution. This is one of very few applications of crosshole ERT for monitoring of gaseous CO_2 injection in a shallow aquifer (Dafflon et al., 2013). The monitoring wells of their complex resistivity tomography in Dafflon et al. (2012) were so far apart that the monitoring system almost degraded into a single well complex resistivity imaging with little resolution in the central region. Our ERT monitoring differs from Auken et al. (2014) and Doetsch et al. (2015) in that (1) we used crosshole ERT instead of surface ERT; (2) our pilot experiment had a shorter injection duration and a much smaller CO_2 injection volume (45 kg in 2 days versus 1600 kg in 72 days); (3) our study focused on small changes during the early stage of gaseous and dissolved CO_2 plume growth; (4) we had ground penetration radar (GPR) data to aid in identification of the likely effect from gaseous CO_2.

The objective of this study was to evaluate the effectiveness of the ERT method for imaging a gaseous and dissolved CO_2 plume in a shallow aquifer during the first 2 days of CO_2 injection and to study the early-time behavior of a controlled gaseous CO_2 release.

2. Experiment descriptions

The pilot CO_2 experiment site is located in Vrøgum, western Denmark (Fig. 1A). The area is an open grass field in a managed pine forest. The injection site is an unconfined, unconsolidated siliciclastic aquifer. The 5 m-thick top layer consists of fine-grain Aeolian sand, underlain by a 5 m-thick layer of poorly sorted glacial sand and subordinate gravel. Below that is a 50 m-thick layer of medium well-sorted marine sand (Cahill and Jakobsen, 2013). Further analysis of five core samples by Lassen et al. (2015) revealed multiple thin layers and lenses: a fine sand layer at a depth between 4.2 and 4.4 m, another fine sand layer between 6.3 and 6.6 m and a coarse grained section with pebbles at 9 m depth (Fig. 1B). The soil grain size generally increases with depth. The layer boundaries may be not accurate due to limited and incomplete core samples. This unconfined sand aquifer has a shallow water table at 1.5 m depth in the spring and at 2 m in the fall. The groundwater flows toward the south-south-west.

Four pilot CO_2 injection experiments were conducted at the same site from October 2011 to September 2012 with a goal to inject 45 kg CO_2 gas in 48 h for each experiment (Lassen et al., 2015). In this study, we analyzed ERT data collected between October 11 and October 14, 2011 from the first experiment. Cahill and Jakobsen (2013) reported the geochemical monitoring results for the same first experiment while Lassen et al. (2015) focused mostly on the third experiment conducted in July 2012.

Three monitoring tools were deployed at the site. Groundwater sampling wells were installed to obtain in situ time lapse water chemistry data (Cahill and Jakobsen, 2013). Cross-borehole ground

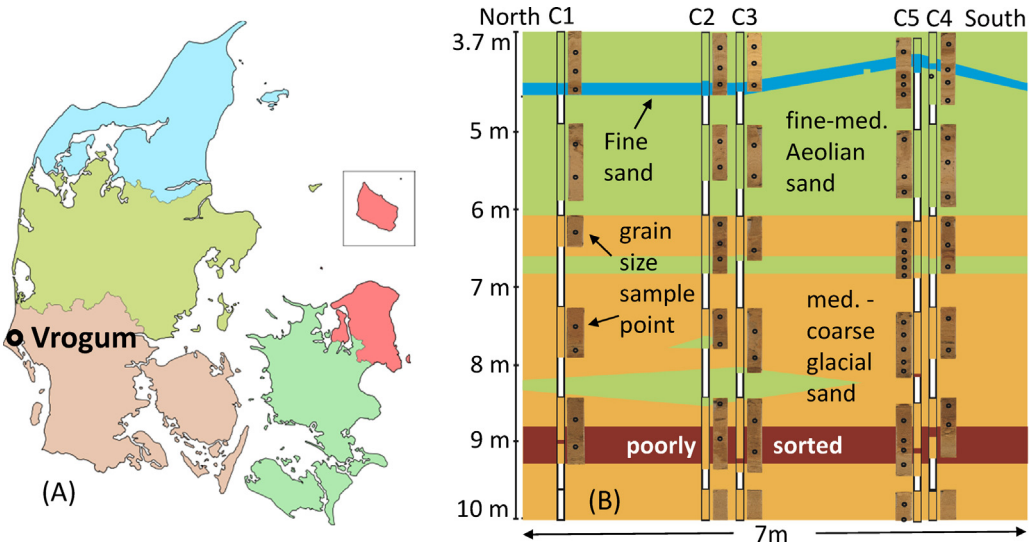

Fig. 1. (A) The CO_2 injection site in Vrøgum, western Denmark. (B) Conceptual geologic model based on the grain size from core logs (adapted from Lassen et al., 2015). C1-C5 are five sediment cores.

penetrating radar (GPR) was employed for tracking migration of gas-phase CO_2 (Lassen et al., 2015). ERT monitored migration of both gaseous and dissolved CO_2. The sampling wells provided 1D point measurements infrequently; the GPR method produced 1D and 2D images of CO_2 gas content, while ERT gave 3D time lapse images of CO_2 distribution with autonomous data collection.

At the experiment site, a 45° angled injection well was screened at 9–9.85 m depth. Two of the 17 sampling points (#1 and #2) for groundwater chemistry were located upflow while the rest were located downflow (Fig. 2). Sampling points were arranged at multiple levels at 2.4 m, 4 m and 8 m depths (Cahill and Jakobsen, 2013). CO_2 gas injection began on October 12, 2011 for 50 h with 45 kg CO_2 being injected. A variable injection rate was used: 10 g/min for the first 24 h, then 20 g/min for the next 24 h, and greater than 20 g/min for additional 2 h.

Fig. 2 shows four of six GPR monitoring boreholes, numbered from GPR1 to GPR4, which were used to monitor migration of

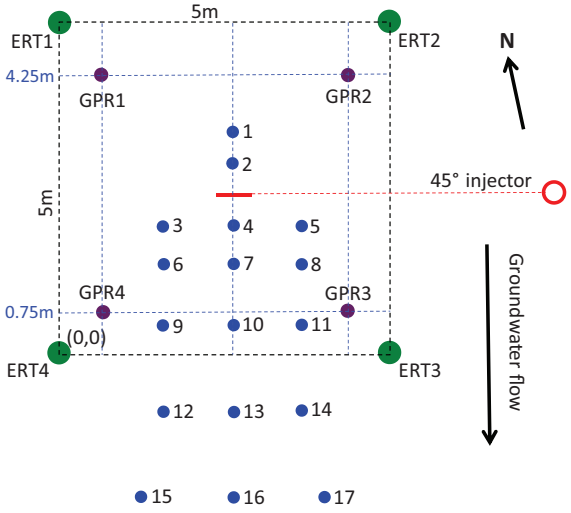

Fig. 2. Layout of monitoring system at the Vrøgum CO_2 injection site (not to scale). #1-#17 are groundwater sampling wells, GPR1-4 stands for ground penetrating radar (GPR) boreholes 1–4, and ERT1-4 stands for electrical resistivity tomography (ERT) boreholes 1–4.

gaseous CO_2 that displaced soil water and reduced soil moisture content and bulk EC. GPR measured the dielectric constant that was converted into moisture content using well-established petrophysical relationships (Topp et al., 1980; Ferré et al., 1996).

Four ERT monitoring boreholes were installed around the screened injection interval for tracking CO_2 plume distribution and migration. They were laid out in a 5 m × 5 m square and labeled as ERT1, ERT2, ERT3 and ERT4 in Fig. 2. Each vertical electrode array permanently installed in a borehole consisted of 24 electrodes at a spacing of 0.5 m from 1.5 m to 13 m depth. There were total 96 electrodes in four ERT boreholes. An ERT measurement was obtained by injecting an electric current (I) from one pair of electrodes and measuring a voltage (V) using another pair of electrodes. ERT data were collected using two different bipole-bipole electrode configurations (Zhou and Greenhalph, 2000). The first array was a horizontal bipole-bipole (HBB) electrode configuration, in which the two transmitting electrodes were located at the same depth and separated in two different wells, and so did the two receiving electrodes. The primary advantage of this HBB array includes large signal strength and high signal to noise ratio (Zhou and Greenhalph, 2000). The HBB configuration has a limited and biased resolution due to the predominance of current flows and potential measurements in the horizontal direction with no data coverage in all other directions. One HBB data set consisted of 5634 measurements, about half of which were reciprocal measurements for evaluation of data quality. It took 47 min to collect one HBB data set. Two baseline data sets were collected on September 28, 2011 (13 days before injection) and October 11, 2011 (1 day before injection). Seven monitoring data sets were collected at 2 h, 8 h, 26 h, 29 h, 30 h, 31 h and 49 h after CO_2 injection began.

The second electrode configuration used for ERT data collection was a Skip4 vertical bipole-bipole (VBB) array that had a bipole length equal to five electrode spacings by skipping four electrodes between two transmitting electrodes and also between two receiving electrodes. A large bipole length enhances the signal strength. The VBB array produced 13343 data points per data set, which also included about 50% reciprocal measurements. It took 110 min to collect one VBB data set. Four VBB data sets were collected at 0 h (baseline data set), 3 h, 24 h and 50 h after CO_2 injection began. Though ERT monitoring lasted for 2 days only, hydrogeochemical monitoring continued for 126 days (Cahill and Jakobsen, 2013).

3. Data analysis methods

ERT data sets went through a quality assurance process in which small measured resistance (abs(V/I) < 1e−4) and data with a large reciprocal error (>3%) were removed, few duplicate observations were stacked, and reciprocal measurements were averaged. This preprocessing method was successfully applied to the ERT monitoring data for deep geologic carbon sequestration (Carrigan et al., 2013; Yang et al., 2014) and it was again used for this shallow aquifer case. Data sets collected with HBB and VBB arrays were preprocessed separately.

The baseline data set was inverted using a least squares smooth model inversion algorithm (LaBrecque et al., 1999) with an objective function given by

$$S(\mathbf{m}) = (\mathbf{d}_{calc} - \mathbf{d}_{meas})^T \mathbf{W}^T \mathbf{W} (\mathbf{d}_{calc} - \mathbf{d}_{meas}) + \boldsymbol{\alpha} (\mathbf{m} - \mathbf{m}_0)^T \mathbf{R}^T \mathbf{R} (\mathbf{m} - \mathbf{m}_0), \quad (1)$$

where $\mathbf{d}_{meas}$ is the measured data and $\mathbf{d}_{calc}$ is the calculated data from a numerical model. $\mathbf{W}$ is a diagonal data weight matrix based on an assumption of uncorrelated Gaussian noise and each diagonal entry is defined by the reciprocal of standard deviation of the corresponding measurement. $\mathbf{m}$ is the resistivity model to be solved. $\mathbf{m}_0$ is an optional prior resistivity model. $\mathbf{R}$ is a first-order difference operator that facilitates calculation of the spatial roughness of a resistivity model. $\boldsymbol{\alpha}$ is a trade-off factor whose role is to balance the influence of data misfit and model roughness in the objective function. The nonlinear inverse problem defined by Eq. (1) was solved deterministically with an iterative Gauss Newton method for subsurface resistivity distribution.

Without measurement error estimates, we assumed that the data standard deviation(s) in the data weight matrix $\mathbf{W}$ consists of two parts (Yang et al., 2014; LaBrecque et al., 1996):

$$s_i^2 = a^2 + b^2 d_i^2, \quad (2)$$

where "a" was often set to a small fraction, e.g., 10%, of the smallest data value and it may account for measurement errors due to ambient noise and limited hardware resolution. The second term includes a factor "b" and the ith data d_i and it may represent physical model and numerical errors, and it is intended to give an equal weight to both small and large data values. This "b" factor was often set to 1–5% for the baseline data and a smaller percentage for a monitoring data set because the difference inversion method can fit a monitoring data set better due to cancellation of coherent noises (LaBrecque and Yang, 2001).

The time lapse monitoring data were inverted using a difference inversion method described by LaBrecque and Yang (2001) with an additional temporal roughness constraint as the third term (Yang et al., 2014) in the objective function below:

$$S(\mathbf{m}) = \Delta\mathbf{d}^T \mathbf{W}^T \mathbf{W} \Delta\mathbf{d} + \boldsymbol{\alpha} (\mathbf{m} - \mathbf{m}_0)^T \mathbf{R}^T \mathbf{R} (\mathbf{m} - \mathbf{m}_0) + (\mathbf{m} - \mathbf{m}_0)^T \boldsymbol{\beta} (\mathbf{m} - \mathbf{m}_0) \quad (3)$$

where the data deviation $\Delta\mathbf{d}$ is given by

$$\Delta\mathbf{d} = \left(\mathbf{d}_{calc} - \mathbf{d}^0_{calc}\right) - \left(\mathbf{d}_{meas} - \mathbf{d}^0_{meas}\right). \quad (4)$$

The superscript 0 in Eq. (4) denotes the baseline data. The regularization factor $\boldsymbol{\beta}$ in Eq. (3) is a diagonal matrix having the same length as the model vector $\mathbf{m}$ and it can be used to prevent drastic resistivity changes from the baseline model and to incorporate prior knowledge into the inversion. The difference inversion method inverts the difference between monitoring and baseline data sets and uses the baseline model as the a priori model. The primary advantage of this method is that the effects of systematic and coherent data noise are mitigated so that fewer inversion artifacts are shown on the difference images. It has the potential to resolve small temporal resistivity changes between the monitoring and baseline data sets.

We used an in-house 3D resistivity forward model and inversion code based on Eqs. (1)–(4) for inversion of baseline and monitoring data sets (LaBrecque et al., 1999; LaBrecque and Yang, 2001; Carrigan et al., 2013).

Soil bulk resistivity is a function of porosity, pore water resistivity and water saturation according to Archie's equation (Archie, 1942):

$$\rho = a \cdot \phi^{-m} \cdot \rho_w \cdot S_w^{-n} \quad (5)$$

where ρ is the bulk resistivity of the soil or rock, ρ_w is the pore fluid resistivity, ϕ is the porosity of the formation, S_w is the water saturation, "n" is the saturation exponent with a default value $n = 2$ for clay-free sands, and "a" and "m" are empirical factors that will be canceled in our derivation below. The empirical Archie's equation describes ion flow in clean consolidated sands. Waxman-Smits equation is better suited to sediments with considerable amount of clay (Waxman and Smits, 1968).

For time lapse ERT monitoring below a water table, the baseline water saturation $S_w = 100\%$ before CO_2 injection. The baseline soil resistivity ρ_0 is given by

$$\rho_0 = a \cdot \phi^{-m} \cdot \rho_{w0} \quad (6)$$

Gas-phase CO_2 displaces water, forms CO_2 bubbles in an aquifer and reduces water saturation. This is similar to the effect of supercritical CO_2 (Carrigan et al., 2013) except that gas-phase CO_2 also dissolves in the water and increases the electrical conductivity (EC) of pore fluid (Cahill and Jakobsen, 2013). Considering that $S_w + S_{CO_2} = 100\%$ and electrical conductivity $\sigma = 1/\rho$, from Eqs. (5) and (6), we obtain the ratio of injection conductivity to preinjection conductivity:

$$\frac{\sigma}{\sigma_0} = \frac{\sigma_w}{\sigma_{w0}} \left(1 - S_{CO_2}\right)^n, \quad (7)$$

where σ_0 is the preinjection baseline soil bulk EC, σ is the bulk EC during CO_2 injection, and σ_{w0} and σ_w are pore fluid conductivities before and during CO_2 injection. As discussed previously, an increase of CO_2 gas saturation (S_{CO_2}) reduces bulk EC but dissolved CO_2 increases pore fluid conductivity and bulk EC. These two concurrent processes have opposite effects on bulk EC and may result in small or no bulk EC changes in the early stage of CO_2 injection. According to Eq. (7), 10% CO_2 gas saturation would result in 19% reduction of bulk EC.

Changes of total dissolved solids (TDS) incurred by CO_2 dissolution have a strong impact on EC of a pore fluid. The water desalination industry often uses the following empirical linear relationship to estimate TDS from EC measurements of water:

$$TDS = K \cdot EC, \quad (8)$$

where the factor K ranges from 0.5 to 0.9 depending on the TDS level (Walton, 1989). The TDS unit is mg/L and EC is in μS/cm at 20 °C. So 10% changes in TDS will result in 10% changes in EC due to their linear relationship.

4. Results

The HBB data had large signal strength and a higher signal to noise ratio than the VBB data. By setting the minimum resistance to 1×10^{-4} Ohm and the maximum reciprocal error to 3%, we filtered out only 1% of HBB data that may be weak signals due to singular electrode configuration (Zhou and Greenhalph, 2000). The HBB data sets left roughly 3350 data points per data set. The VBB data were noisier and about 7% of the data were removed during preprocessing. The VBB data left about 6350 data points per data set. We combined the HBB and VBB data sets that were collected

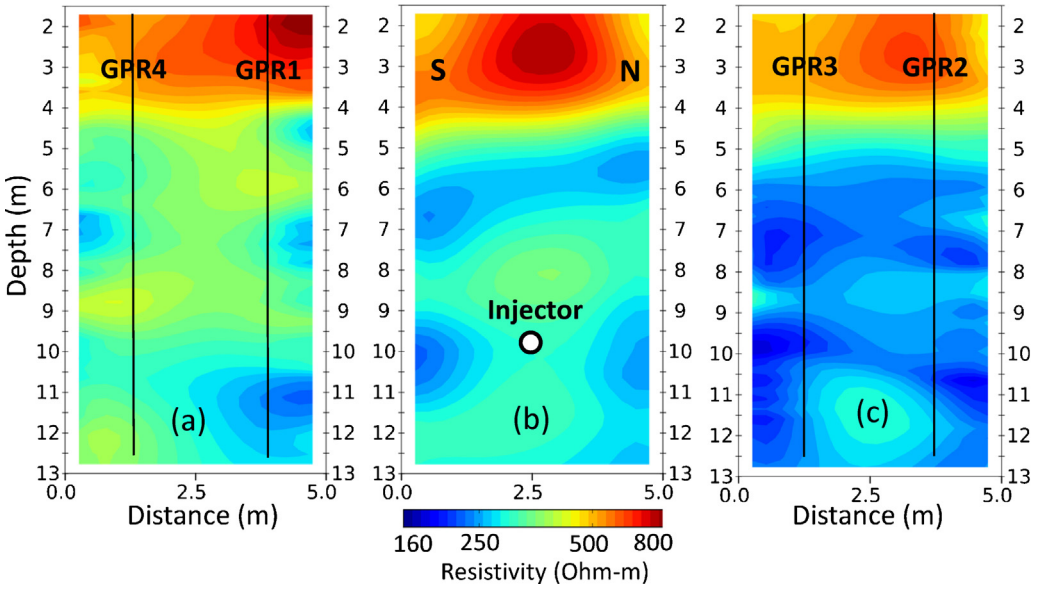

Fig. 3. The baseline electrical resistivity model from the combined HBB and VBB baseline data set. Three south (S) – north (N) cross-sections intersect (a) GPR4-GPR1, (b) injector and (c) GPR3-GPR2 respectively.

consecutively into a single data set. Because there were only four VBB data sets, we ended up with one preinjection baseline data set and three monitoring data sets with starting acquisition times at 2 h, 24 h and 49 h. Each combined data set took about 3 h to collect. The combined data sets were inverted for presumably higher spatial resolution with reduced temporal resolution due to longer data collection time. We also inverted 8 HBB data sets separately for higher temporal resolution.

The preinjection baseline data were inverted using a smooth model inversion algorithm described by Eqs. (1) and (2). The 3D forward modeling mesh consists of 120,032 cells ($44 \times 44 \times 62$). The inversion took about 9 min for the baseline data set (about 9700 data points) and 3 min for a monitoring data set on a 12-core node of a Linux cluster.

Three south-north vertical cross-sections of the baseline resistivity model are shown in Fig. 3 for the combined data. The cross-sections intersect GPR boreholes for easy comparison with GPR data (Lassen et al., 2015). It is apparent that top 13 m of the site consist of two primary layers. The upper 5 m-thick Aeolian sand layer has a high resistivity value over 500 Ohm-m. The lower layer of glacial sand is more conductive with a relatively large resistivity variation between 160 Ohm-m and 500 Ohm-m, indicating the lateral and vertical heterogeneities due to thin layers and lenses (Fig. 1). The layer boundary between poorly sorted glacial sand and medium well-sorted marine sand at 10 m depth (Cahill and Jakobsen, 2013) was only vaguely visible in Fig. 3 and it did not show a large resistivity contrast. The more conductive east side along the boreholes GPR2 and GPR3 may suggest higher porosity and higher moisture content (Fig. 3c). The layer structure of cross-sections implies lateral soil homogeneity along the groundwater flow direction. The vague discontinuity at about 9 m may be the signature of a thin poorly sorted layer (Fig. 1).

The difference inversion of combined data sets revealed that bulk EC along a diagonal cross-section between boreholes ERT2 and ERT4 increased with time for the first 49 h since CO_2 injection began on October 12, 2011 (Fig. 4). It is obvious that the dissolved CO_2 had a greater effect on the bulk EC than the gaseous CO_2 (Eq. (7)) so that the increase of bulk EC dominated the images. The growth of a CO_2 plume appeared to be confined in the middle glacial sand layer between 5 m and 11 m mostly above the injection point. Most of the CO_2 plume was skewed toward ERT2 against the direction of groundwater flow. In 49 h, the bulk EC increased up to 10%. Fig. 5 provides a 3D view of the CO_2 plume growth. Most of the CO_2 plume was located to the northeastern part around the borehole ERT2 and some CO_2 must therefore be expected to have migrated outside the ERT imaging volume. Two lenses of bulk EC reduction were observed around ERT3 (Fig. 5c) where the effect of gaseous CO_2 may have overwhelmed that of dissolved CO_2.

Inversion of more frequently sampled VBB data sets provides a higher temporal resolution of the CO_2 plume growth (Fig. 6). At the 2-h and 8-h marks, a weak conductive anomaly was detected due to apparent low injection rate of 10 g/min and the opposite effects of gaseous and dissolved CO_2. After increasing injection rate to 20 g/min at the 24-h mark, a strong anomaly of bulk EC increase was observed above the injection point at the 26-h mark and it then migrated toward ERT2 preferentially. The images of bulk EC changes at 26 h, 29 h and 31 h show little difference within 5 h. The maximum bulk EC change was reached at the 49-h mark, the end of ERT monitoring.

Some negative bulk EC changes were observed and most of them are scattered around ERT electrodes (Figs. 4–6). Two relatively larger negative EC anomalies clung to ERT3 in Fig. 5 are the effect of gaseous CO_2. The remaining small low-magnitude negative changes may be artifacts due to the noise because a transmitting electrode in an automated data acquisition system may be used as a receiving one too soon without giving enough time for a charged electrode being discharged. A thin-layer EC increase at 1.5 m depth at 26 h, 29 h and 31 h may be caused by the fluctuation of water table that is at approximately 1.8 m depth (Fig. 6).

GPR can resolve soil porosity and CO_2 gas content (Lassen et al., 2015). We compare CO_2 gas saturation estimated from GPR zero-offset-profiling (ZOP) data with the bulk EC changes from ERT along four GPR transects: GPR1-GPR2 (Fig. 7), GPR2-GPR3 (Fig. 8), GPR3-GPR4 (Fig. 9) and GPR1-GPR4 (Fig. 10). An ERT depth profile was obtained by averaging EC changes at the same depth on an ERT vertical cross-section. The data for comparison were collected about 2 days since injection began. Fig. 7 shows that gaseous and dissolved CO_2 anomalies are centered at the 7 m depth. The effect of dissolved CO_2 is much stronger and broader than that of gaseous CO_2, so that the bulk EC shows a larger EC increase. The opposite effects of gaseous and dissolved CO_2 are apparent along the GPR2-GPR3 and GPR3-GPR4 transects where a high CO_2 gas saturation

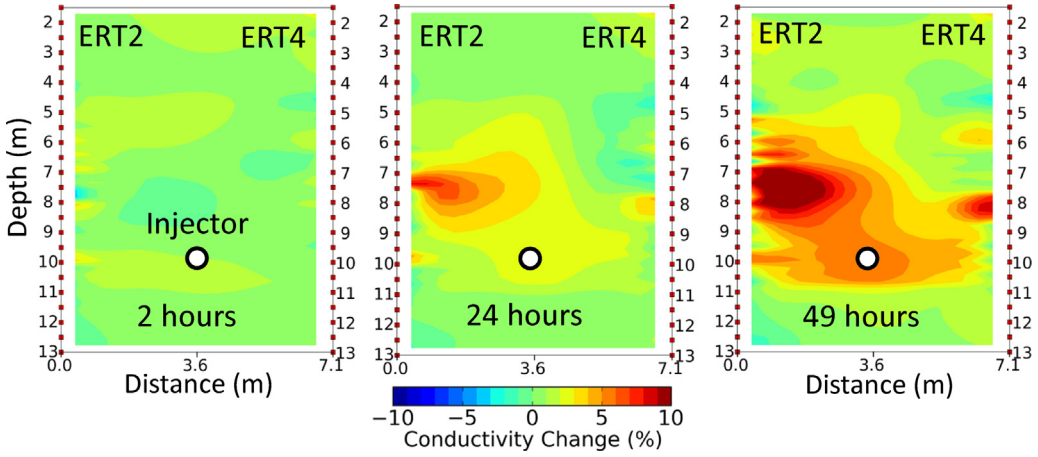

Fig. 4. Time lapse electrical conductivity changes along a diagonal cross-section between boreholes ERT2 and ERT4 from combined HBB and VBB data.

corresponds to a low bulk EC increase and vice versa (Figs. 8 and 9). When the CO_2 gas saturation is very high (>25%), the effect of resistive gaseous CO_2 cancels that of conductive dissolved CO_2 and the bulk EC changes are either small or negative (Fig. 9). Both GPR and ERT data agree that little CO_2 migrated to the west along the transect GPR1-GPR4 (Fig. 10).

Both ERT and water sampling measure electrical conductivity (EC). Fig. 11 shows their similarity and difference. Both methods detected a comparable magnitude of an EC increase at sampling points 2, 5 and 8 that are on the preferential pathway of CO_2 migration, but they show a significant difference in EC changes at sampling points 1 and 7. The water sample EC data at points 3 and 6 are not available to authors, but Fig. 4 in Cahill and Jakobsen (2013) provides a comprehensive view of dissolved CO_2 plume.

5. Discussions

ERT can detect combined effects of both gaseous and dissolved CO_2. However, it cannot separate the effect of dissolved CO_2 from that of gaseous CO_2. The dominance of positive bulk EC changes on ERT difference images indicates that dissolved CO_2 had a larger effect on the bulk EC than the gaseous CO_2. Therefore, the ERT method tracks primarily the migration of a dissolved CO_2 plume that is often larger spatially than a gaseous CO_2 plume (Lamert et al., 2012).

The primary factors that control the migration of a CO_2 plume consist of buoyancy of gaseous CO_2, sediment heterogeneity, groundwater flow and external pressure exerted by the injector. The CO_2 plume at the Vrøgum site migrated mostly upward due to buoyancy (Figs. 4–6). It also skewed toward northeastern region by overcoming local groundwater flow. The eastern part between boreholes ERT2 and ERT3 is more porous (Lassen et al., 2015) and may be more permeable. It became the preferential pathway for the CO_2 plume. The CO_2 plume was trapped within the slightly more porous glacial sand layer between 5 m and 10 m depths (Figs. 4 and 6). The top confining layer was fine-medium Aeolian sand. CO_2 did not leak into the lower layer due to the buoyancy of gaseous CO_2 and a layer boundary between the upper glacial sand and lower marine sand at about 10 m depth (Cahill and Jakobsen, 2013). It is important to point out that no local regularization was

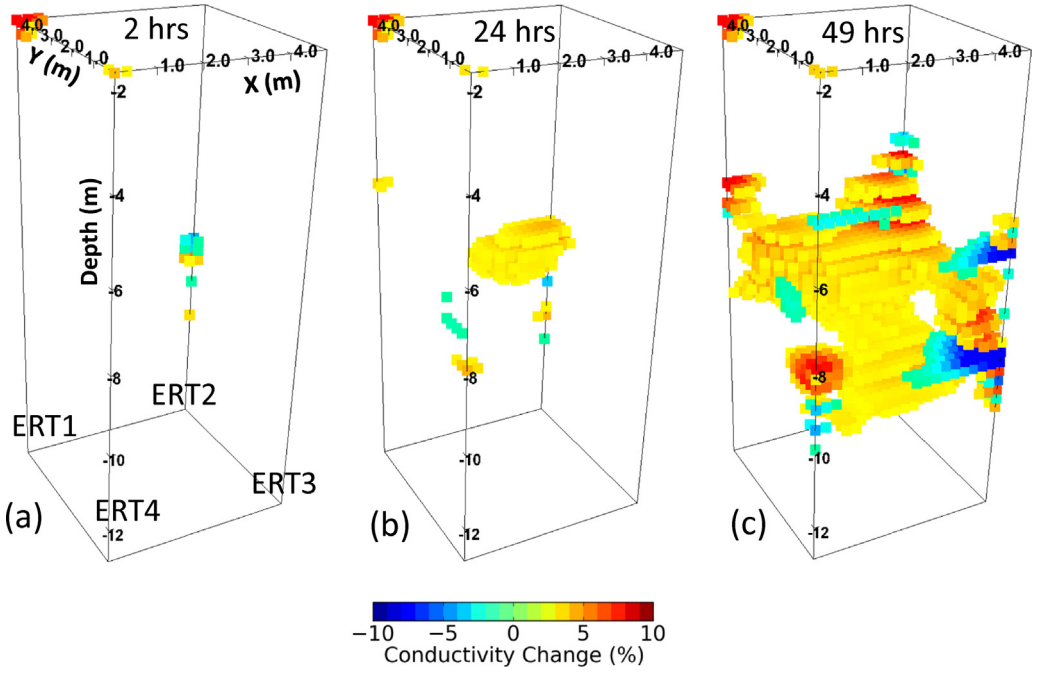

Fig. 5. 3D Time lapse electrical conductivity (EC) changes from combined HBB and VBB data. The bulk EC changes within [−3%, 5%] were turned transparent.

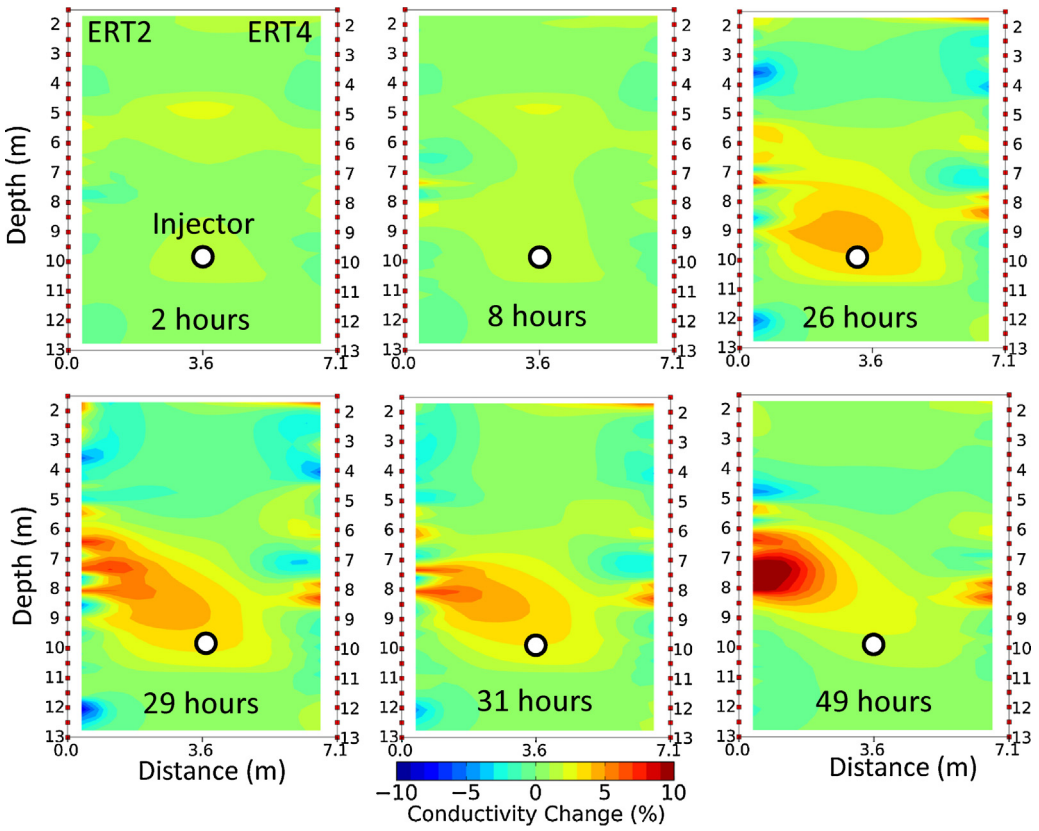

Fig. 6. Time lapse electrical conductivity changes along a diagonal cross-section between boreholes ERT2 and ERT4 from HBB data.

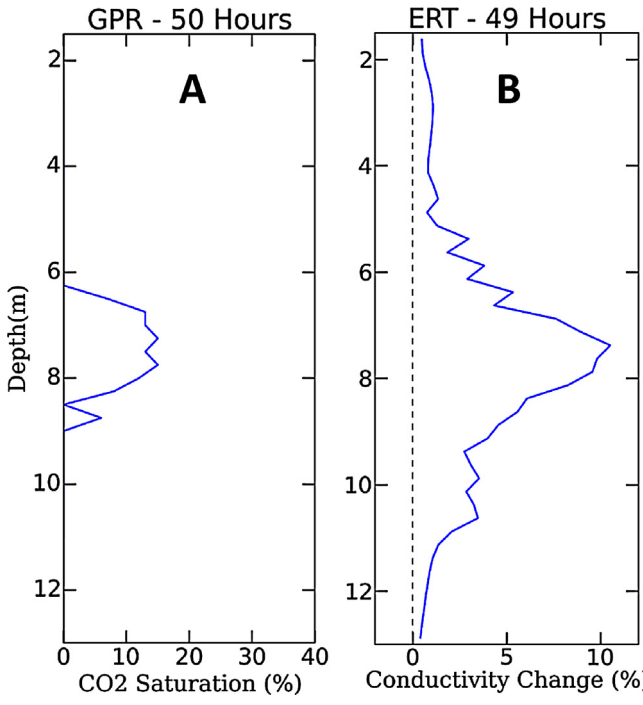

Fig. 7. Comparison between GPR-derived CO_2 gas saturation (A) and ERT-derived EC changes (B) along the transect between GPR1 and GPR2 after 2-day CO_2 injection. ERT data are from combined HBB and VBB arrays and GPR data are from zero offset profiling (ZOP).

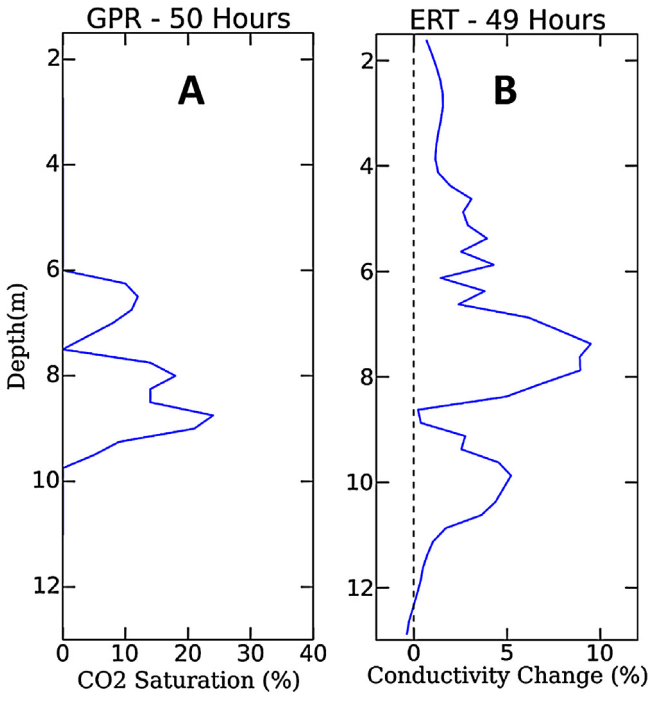

Fig. 8. Comparison between GPR-derived CO_2 gas saturation (A) and ERT-derived EC changes (B) along the transect between GPR2 and GPR3 after 2-day CO_2 injection.

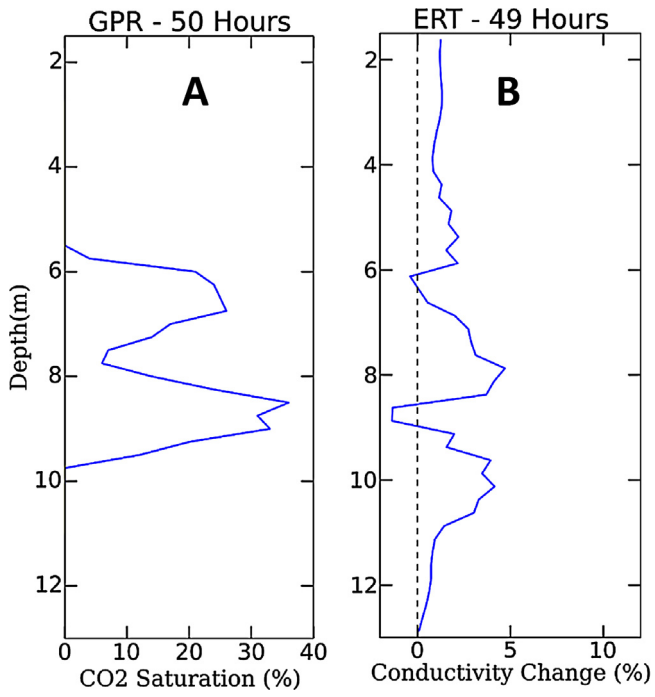

Fig. 9. Comparison between GPR-derived CO_2 gas saturation (A) and ERT-derived EC changes (B) along the transect between GPR3 and GPR4 after 2-day CO_2 injection.

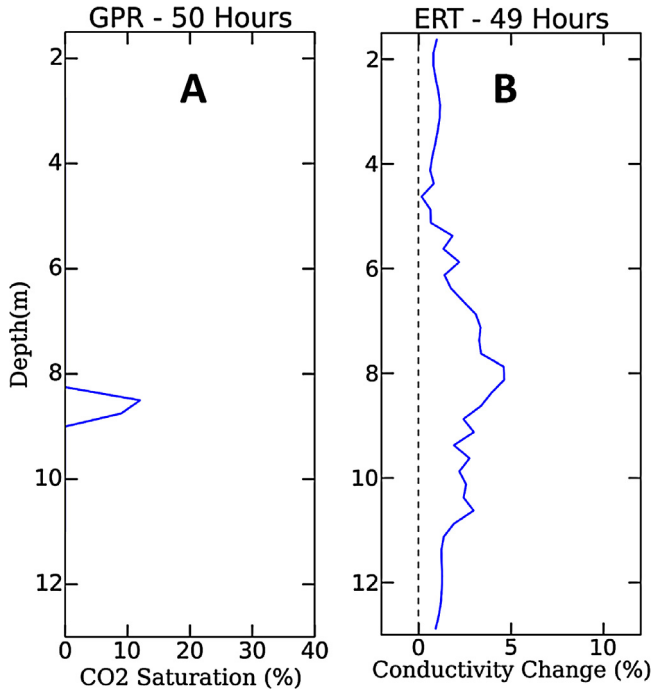

Fig. 10. Comparison between GPR-derived CO_2 gas saturation (A) and ERT-derived EC changes (B) along the transect between GPR1 and GPR4 after 2-day CO_2 injection.

imposed in the ERT inversion to constrain the CO_2 plume within the glacial sand layer.

The CO_2 plume migrated mostly to the northeast against groundwater flow direction during the first 2 days of CO_2 injection because of the large pressure exerted by the injector. After the injection stopped at the 50-h mark, Cahill and Jakobsen (2013) observed that the groundwater flow gradient became the primary driving force. The CO_2 plume migrated along the groundwater flow direction and grew much larger to the south and outside ERT

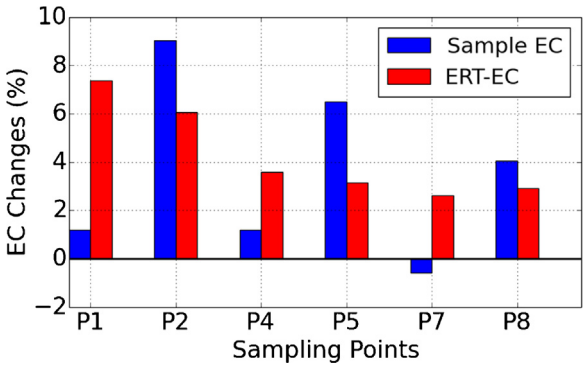

Fig. 11. Comparison of EC changes at 8 m depth between in situ water samples at the 50-h mark and combined HBB and VBB ERT data at the 49-h mark.

imaging volume. Unfortunately, we do not have ERT data beyond the 50-h mark.

The gaseous CO_2 plume measured with GPR (Lassen et al., 2015) had a similar migration pathway to that of dissolved CO_2. Both ERT data and zero-offset-profiling (ZOP) GPR data detected the CO_2 plume within the same depth range along north, east and south transects (Figs. 7–9), but little CO_2 along the GPR1-GPR4 transect to the west (Fig. 10). Figs. 8 and 9 clearly show that ERT detected the opposite effects from gaseous and dissolved CO_2 because a high CO_2 gas saturation always corresponds to a small or negative bulk EC change. The dissolved CO_2 plume estimated from ERT data are located between 5 m and 11 m depths, much larger than the depth range (6–9 m) of the gaseous CO_2 plume by ZOP GPR data. This difference may have resulted from the smooth model inversion of ERT data which often underestimates the magnitude and overestimates the extent of anomalies (Day-Lewis et al., 2005).

ERT is a geophysical imaging method and it resolves the bulk EC of pore water, gaseous CO_2 and soil matrix, but water sampling measures EC of a gas-free water sample from a sampling point. That may explain the similarity and difference between ERT and water sampling data in Fig. 11. Our ERT results in Fig. 11 agree well with Fig. 4 in Cahill and Jakobsen (2013) which shows that the sampling points 2, 5 and 8 are inside the CO_2 plume and the sampling points 1, 4 and 7 are on the edge of the plume. Auken et al. (2014) obtained similar results that both ERT and water sampling can delineate the dissolved CO_2 plume, but the water sampling data demonstrates some fine-scale variations while the ERT image is much smoother.

GPR ZOP data detected gaseous CO_2 around GPR2 in 2 h after injection began (Lassen et al., 2015). Volumetric CO_2 gas content reached 5% in 4 h and 10% after 25 h injection. However, ERT detected only a minute EC increase at the 8-h mark (Fig. 6) because the EC increase in a noncarbonate aquifer due to CO_2 intrusion was too slow to be detectable (Fahrner et al., 2011) and the effects from gaseous and dissolved CO_2 might have canceled each other.

CO_2 gas content showed a monotonic increase during the first 21-h CO_2 injection and then remained fairly constant afterwards (Lassen et al., 2015). However, water EC can have a monotonic increase for more than 20 days (Cahill and Jakobsen, 2013; Trautz et al., 2013). Both dissolved CO_2 and gaseous CO_2 increased in tandem and their effects on electrical conductivity canceled each other for the first 24 h. CO_2 gas content remained almost constant after 24 h and then the bulk EC increased more rapidly. This explains that bulk EC increase was much smaller for the first 24 h than that at the 50-h mark (Figs. 4–6).

The fluctuation of groundwater table can incur significant EC changes near the water table. We observed an EC increase between 26 and 31 h (Fig. 6) due to a rising water table that could be a seasonal change or was caused by the increase of injection rate. Auken et al. (2014) detected an EC decrease most likely due to a

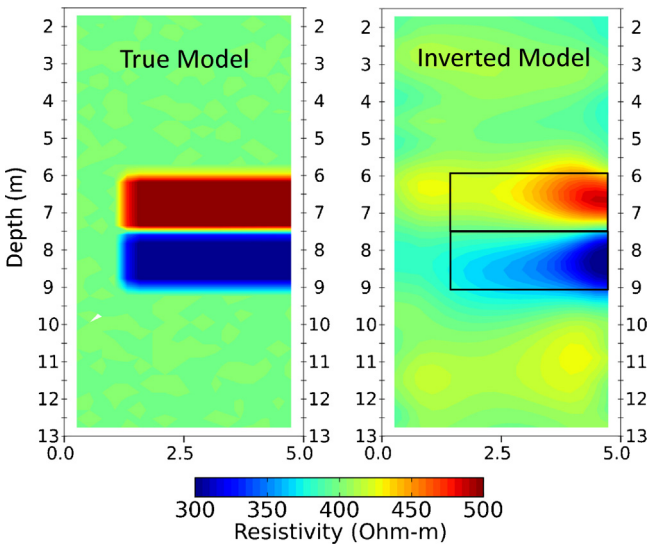

Fig. 12. Synthetic model study of ERT resolution between a 300 Ohm-m conductor and a 500 Ohm-m resistor in a 400 Ohm-m half space. Electrode layout and measurement arrays are the same as those at the Vrøgum site.

lowering water table in the fall. They attributed the EC decrease to the fluctuating water saturation in the vadose zone due to drying and precipitation events.

The maximum bulk EC increase detected by ERT was about 10% at the 49-h mark. These small changes could be overwhelmed by a few percent of noise in ERT data. Although the bulk EC change was small, temporal EC changes were consistent and detectable by ERT thanks to the low-noise data and the difference inversion algorithm that suppresses coherent noise and enhances small EC changes.

With a high CO_2 gas saturation (15–30%) in Figs. 7–9 and less than 10% water EC increase at the Vrøgum site (Fig. 11), the estimated bulk EC changes using Eq. (7) should be mostly negative instead of positive in Figs. 7–9, an apparent disagreement between GPR and ERT data. In Fig. 7, the maximum gas saturation is around 15% and the maximum bulk EC change is 10%. According to Eq. (7), it requires a 52.2% increase in water EC to reach 10% bulk EC increase. In Fig. 9, a 202% increase in water EC is needed to cancel the effect of 30% gas saturation. However, the maximum water EC increase is only 9% in Fig. 11. These seemingly significant differences have multiple causes. At first, all water EC sampling points are either outside or near the edge of the CO_2 plume that is around ERT2 (Fig. 2). It is very likely that the water EC increase reached 52.2% along the transect GPR1-GPR2 in Fig. 7 because Cahill and Jakobsen (2013) reported that the maximum water EC increase can be as high as 83% during the same test, which is still far below the expected 202% increase in water EC in Fig. 9. Secondly, ERT has limited and variable spatial resolution and cannot resolve the true earth resistivity (Day-Lewis et al., 2005). In particular, it is less sensitive to a resistive gaseous CO_2 anomaly (Fig. 12). Thirdly, it is also possible that the smaller resistive gaseous CO_2 plume is wrapped and electrically shielded by the broader conductive dissolved CO_2 plume, which renders the resistive gas plume undetectable. Saribudak (2012) did not detect any resistive anomaly over an air-filled cave due to conductive moisture and mineralization around the cave. Maillol et al. (1999) also found that ERT could not detect resistive dry voids but it was effective in locating conductive water-filled voids. Fourthly, there is no direct and proportional one-to-one mapping from water EC to the bulk EC (Fig. 11) because they sample different materials with significantly different sampling volumes (Auken et al., 2014). Lastly, the GPR method may overestimate CO_2 gas saturation that is not calibrated and the Archie's equation breaks due to the limited and variable ERT resolution and some clay at the site.

ERT monitoring for this pilot experiment can be improved by expanding the monitored area to cover the plume growth to the north and east sides and extending ERT data collection beyond 2 days for tracking CO_2 plume migration under natural groundwater flow without injection. The extent of the CO_2 plume and magnitude of EC changes grew much larger later (Cahill and Jakobsen, 2013).

The large difference between the HBB data (Fig. 6) and combined HBB and VBB data (Fig. 4) at the 49-h mark was caused by different model resolutions of two data sets. Electrode configuration can be optimized for efficient data acquisition and optimal resolution (Stummer et al., 2004; Zhou and Greenhalph, 2000). We also observed near-surface noise and many inversion artifacts. These findings revealed considerable amount of uncertainties in ERT monitoring results that depend on the electrode configuration, amount of noise in the data, numerical errors, inversion algorithm and constraints, etc. (Yang et al., 2014; Day-Lewis et al., 2005).

Our time lapse ERT monitoring design lacked an optimized survey layout with high spatial and high temporal resolutions (Stummer et al., 2004; Furman et al., 2004; Wilkinson et al., 2006; Loke et al., 2010; Al Hagrey, 2012). An additional requirement for the optimal survey design is to avoid measuring a voltage with an electrode that is just used to inject current because a charged electrode may take tens of minutes to discharge (Dahlin, 2000). Both HBB and VBB arrays used in this study were not optimized for efficient data acquisition and optimal spatial resolution. Combining these two data sets into a single one may or may not improve the model resolution depending on the noise level and distribution, but it surely increased data acquisition time significantly. One HBB data set with 5634 readings took 47 min to collect and one VBB data set with 13,343 readings took 110 min. A combined HBB-VBB data set would take almost 3 h to collect, which degrades the temporal resolution needed for imaging rapid early-time changes. An optimized survey design may achieve the similar resolution of a combined data set with less than 1 h of data collection time instead of 3 h.

ERT appeared to be an effective tool for detection of a CO_2 plume in a controlled release. ERT monitoring offered a competitive advantage over hydrogeochemical sampling and GPR methods because of its high spatial and temporal resolution and unattended data acquisition (Carrigan et al., 2013). However, bulk EC can be affected by many factors such as gaseous CO_2, dissolved CO_2, rainfalls (Zhou et al., 2012) and complex leaking scenarios (Keating et al., 2010). Monitoring a large area is still a daunting task because ERT requires many closely spaced boreholes. Alternative solutions for monitoring a large area include surface ERT (Auken et al., 2014), controlled source electromagnetics method (Girard et al., 2011), and airborne electromagnetics (Costard and Paine, 2015; Dethlefsen et al., 2013).

6. Conclusions

Our study demonstrates that 3D crosshole ERT successfully detected distribution and migration of a CO_2 plume in a shallow unconfined siliciclastic aquifer. The preinjection baseline resistivity model showed a two-layer structure of the site. The electrically more conductive northeast side is more porous and more permeable and it becomes a preferential pathway for the CO_2 plume. ERT is sensitive to the combined effects from conductive dissolved CO_2 and resistive gaseous CO_2. The CO_2 plume migrated upward at the beginning due to buoyancy and toward the northeast direction against the groundwater flow for the first 2 days during the CO_2 injection. The CO_2 plume was confined in the poorly sorted glacial sand layer by the fine grain Aeolian sand at the top and well-sorted marine sand at the bottom. ERT data shows a broader CO_2 plume while water sampling EC had higher fine-scale variability.

The positive bulk EC change was small (<10%) but dominated ERT difference images. The bulk EC changes from ERT agreed partially with water EC and GPR data. The apparent disagreement between high CO_2 gas saturation and prevailing positive bulk EC changes may be caused by limited and variable ERT resolution, low ERT sensitivity to resistive anomalies and uncalibrated CO_2 gas saturation. The good quality data and effective difference inversion algorithm helped detect small changes of bulk EC. ERT monitoring offered a competitive advantage over 1D water sampling and 2D GPR imaging because it provided 3D time lapse tomographic images of CO_2 distribution with autonomous data collection. Our electrode configuration can be optimized for more efficient data acquisition and better spatial resolution.

Acknowledgments

This work was performed under the auspices of the U.S. Department of Energy by Lawrence Livermore National Laboratory (LLNL) under Contract DE-AC52-07NA27344. LLNL IM release number is LLNL-JRNL-653565. The study was funded partially by a grant from the Danish Strategic Research Council for the project Environmental Technology for Geological Storage of Carbon Dioxide, under contract no.: 09-067246. Special thanks to the many helpers who assisted in the field data collection.

References

Al Hagrey, S.A., 2012. 2D optimized electrode arrays for borehole resistivity tomography and CO_2 sequestration modeling. Pure Appl. Geophys. 169, 1283–1292.

Archie, G.E., 1942. The electrical resistivity log as an aid in determining some reservoir characteristics. Trans. Am. Inst. Mining Mettall. Eng. 146, 54–61.

Auken, E., Doetsch, J., Fiandaca, G., Christiansen, A.V., Gazoty, A., Cahill, A.G., Jakobsen, R., 2014. Imaging subsurface migration of dissolved CO_2 in a shallow aquifer using 3D time lapse electrical resistivity tomography. J. Appl. Gerontol. 101, 31–41.

Bergmann, P., Schmidt-Hattenberger, C., Kiessling, D., Rücker, C., Labitzke, T., Henninges, J., Baumann, G., Schütt, H., 2012. Surface-downhole electrical resistivity tomography applied to monitoring of CO_2 storage at Ketzin, Germany. Geophysics 77, B253–B267, http://dx.doi.org/10.1190/geo2011-0515.1.

Cahill, A.G., Jakobsen, R., 2013. Hydro-geochemical impact of CO_2 leakage from geological storage on shallow potable aquifers: a field scale pilot experiment. Int. J. Greenh. Gas Control 19, 678–688.

Cahill, A.G., Marker, P., Jakobsen, R., 2014. Hydrogeochemical and mineralogical effects of sustained CO_2 contamination in a shallow sandy aquifer: a field scale controlled release experiment. Water Resour. Res. 50, 1735–1755, http://dx.doi.org/10.1002/2013WRD014294.

Carrigan, C.R., Yang, X., LaBrecque, D.J., Larsen, D., Freeman, D., Ramirez, A.L., Daily, W., Aines, R., Newmark, R., Friedmann, S.J., Hovorka, S., 2013. Electrical resistivity tomographic monitoring of CO_2 movement in deep geologic reservoirs. Int. J. Greenh. Gas Control 18, 401–408.

Carroll, S.A., Keating, E., Mansoor, K., Dai, Z., Sun, Y., Trainor-Guitton, W., Brown, C., Bacon, D., 2014. Key factors for determining groundwater impacts due to leakage from geologic carbon sequestration reservoirs. Int. J. Greenh. Gas Control 29, 153–168.

Costard, L., Paine, J.G., 2015. Characterizing initial state conductivity distribution at a CO2 injection site with airborne, surface, and borehole electromagnetic induction methods. In: Symposium on the Application of Geophysics to Engineering and Environmental Problems (SAGEEP), Austin, Texas, March 22-26, pp. 360–368.

Dafflon, B., Wu, Y., Hubbard, S.S., Birkholzer, J.T., Daley, T.M., Pugh, J.D., Peterson, J.E., Trautz, R.C., 2013. Monitoring CO_2 intrusion and associated geochemical transformations in a shallow groundwater system using complex electrical methods. Environ. Sci. Technol. 47, 314–321.

Dahlin, T., 2000. Short note on electrode charge-up effects in DC resistivity data acquisition using multi-electrode arrays. Geophys. Prospect. 48, 181–187.

Denchik, N., Pezard, P.A., Neyens, D., Lofi, J., Frederick, G., Girard, J., Levannier, A., 2014. Near-surface CO_2 leak detection monitoring from downhole electrical resistivity at the CO_2 Field Laboratory, Svelvik Ridge (Norway). Int. J. Greenh. Gas Control 28, 275–282.

Dethlefsen, F., Kober, R., Schafer, D., al Hagrey, S.A., Hornbruch, G., Ebert, M., Beyer, M., Grobmann, J., Dahmke, A., 2013. Monitoring approaches for detecting and evaluating CO_2 and formation water leakages into near-surface aquifers. Energy Procedia 37, 4886–4893.

Day-Lewis, F.D., Singha, K., Binley, A.M., 2005. Applying petrophysical models to radar travel time and electrical resistivity tomograms: resolution-dependent limitations. J. Geophys. Res. 110, B08206, http://dx.doi.org/10.1029/2004JB003569.

Doetsch, J., Fiandaca, G., Auken, E., Christiansen, A.V., Cahill, A.G., Jakobsen, R., 2015. Field-scale time-domain spectral induced polarization monitoring of geochemical changes induced by injected CO_2 in a shallow aquifer. Geophysics 80, WA113–WA129.

Fahrner, S., Schaefer, D., Dahmke, A., 2011. Reactive transport modeling to assess geochemical monitoring for detection of CO_2 intrusion into shallow aquifers. Energy Procedia 4, 3155–3162, http://dx.doi.org/10.1016/j.egypro.2011.02.230.

Ferré, P.A., Rudolph, D.L., Kachanoski, R.G., 1996. Spatial averaging of water content by time domain reflectometry: implication for twin rod probes with and without dielectric coatings. Water Resour. Res. 32, 271–279.

Furman, A., Ferre, T.P.A., Warrick, A.W., 2004. Optimization of ERT surveys for monitoring transient hydrological events using perturbation sensitivity and genetic algorithms. Vadose Zone Hydrol. 3, 1230–1239.

Girard, J.F., Coppo, N., Rohmer, J., Bourgeois, B., Naudet, V., Schmidt-Hattenberger, C., 2011. Time lapse CSEM monitoring of the Ketzin (Germany) CO_2 injection using 2xMAM configuration. Energy Procedia 4, 3322–3329.

Keating, E.H., Fessenden, J., Kanjorski, N., Koning, D.J., Pawar, R., 2010. The impact of CO_2 on shallow groundwater chemistry: observations at a natural analog site and implications for carbon sequestration. Environ. Earth Sci. 60 (3), 521–536.

Kharaka, Y.K., Thordsen, J.J., Kakouros, E., Ambats, G., Herkelrath, W.N., Beers, S.R., Birkholzer, J.T., Apps, J.A., Spycher, N.F., Zheng, L., Trautz, R.C., Rauch, H.W., Gullichson, K.S., 2010. Changes in the chemistry of shallow groundwater related to the 2008 injection of CO_2 at the ZERT field site, Bozeman, Montana. Environ. Earth Sci. 60 (2), 273–284.

Kiessling, D., Schmidt-Hattenberger, C., Schuett, H., Schilling, F., Krueger, K., Schoebel, B., Danckwardt, E., Kummerow, J., the CO_2 SINK Group, 2010. Geoelectrical methods for monitoring geological CO_2 storage: first results from cross-hole and surface—downhole measurements from the CO_2 SINK test site at Ketzin (Germany). Int. J. Greenh. Gas Control 4 (5), 816–826.

LaBrecque, D.J., Miletto, M., Daily, W., Ramirez, A., Owen, E., 1996. The effects of noise on Occam's inversion of resistivity tomography data. Geophysics 61 (2), 538–548.

LaBrecque, D.J., Yang, X., 2001. Difference inversion of ERT data: a fast inversion method for 3D in situ monitoring. J. Environ. Eng. Geophys. 6, 83–90.

LaBrecque, D.J., Morelli, G., Daily, W.D., Ramirez, A.L., Lundegard, P., 1999. Occam's inversion of 3D ERT data. In: Oristaglio, M., Spies, B. (Eds.), Three-dimensional Electromagnetics, Geophysical Development No. 7. Society of Exploration Geophysicists, pp. 575–590.

Lamert, H., Geistlinger, H., Werban, U., Schütze, C., Peter, A., Hornbruch, G., Schulz, A., Pohlert, M., Kalia, S., Beyer, M., Großmann, J., Dahmke, A., Dietrich, P., 2012. Feasibility of geoelectrical monitoring and multiphase modeling for process understanding of gaseous CO_2 injection into a shallow aquifer. Environ. Earth Sci. 67 (2), 447–462.

Lassen, R.N., Looms, M.C., Sonnenborg, T.O., Jensen, K.H., 2015. Monitoring CO_2 gas-phase injection in a shallow sand aquifer using cross-borehole ground penetrating radar. Int. J. Greenh. Gas Control 37, 287–298.

Le Roux, O., Cohen, G., Loisy, C., Laveuf, C., Delaplace, P., Magnier, C., Rouchon, V., Cerepi, A., Garcia, B., 2013. The CO_2 Vadose project: Time lapse geoelectrical monitoring during CO2 diffusion in the carbonate vadose zone. Int. J. Greenh. Gas Control 16, 156–166 (2013).

Lions, J., Devau, N., de Lary, L., Dupraz, S., Parmentier, M., Gombert, P., Dictor, M., 2014. Potential impacts of leakage from CO_2 geological storage on geochemical processes controlling fresh groundwater quality: a review. Int. J. Greenh. Gas Control 22, 165–175.

Loke, M.H., Wilkinson, P.B., Chambers, J.E., 2010. Fast computation of optimized electrode arrays for 2D resistivity surveys. Comput. Geosci. 36, 1414–1426.

Maillol, J.M., Sequin, M.K., Gupta, O.P., Akhauri, H.M., Sen, N., 1999. Electrical resistivity tomography survey for delineating uncharted mine galleries in West Bengal. India 47, 103–116.

Pettinelli, E., Passeretta, A., Cereti, A., Menghini, A., Annunziatellis, A., Beaubien, S.E., Ciottoli, G., Lombardi, S., 2004. GPR and EM31 investigations on an active CO_2 gas vent. In: 10th Int. Conf. on Ground PenetratingRadar, pp. 563–566.

Saribudak, M., 2012. Do air-filled caved cause high resistivity anomalies? a six-case study from the Edwards Aquifer recharge zone in San Antonio. Houston Geological Society Bulletin, Texas, pp. 41–48.

Schmidt-Hattenberger, C., Bergmann, P., Bösing, D., Labitzke, T., Möller, M., Schröder, S., Wagner, F., Schütt, H., 2013. Electrical resistivity tomography (ERT) for monitoring of CO_2 migration - from tool development to reservoir surveillance at the Ketzin pilot site. Energy Procedia 37, 4268–4275, http://dx.doi.org/10.1016/j.egypro.2013.06.329.

Strazisar, B.R., Wells, A.W., Diehl, J.R., Hammack, R.W., Veloski, G.A., 2009. Near-surface monitoring for the ZERT shallow CO_2 injection project. Int. J. Greenhouse Gas Control 3 (6), 736–744.

Stummer, P., Maurer, H., Green, A.G., 2004. Experimental design: electrical resistivity data sets that provide optimum subsurface information. Geophysics 69, 120–139.

Topp, G.C., Davis, J.L., Annan, A.P., 1980. Electromagnetic determination of soil water content: measurements in coaxial transmission lines. Water Resour. Res. 16, 574–582, http://dx.doi.org/10.1029/WR016i003p00574.

Trautz, R.C., Pugh, J.D., Varadharajan, C., Zheng, L., Bianchi, M., Nico, P.S., Spycher, N.F., Newell, D.L., Esposito, R.A., Wu, Y., Dafflon, B., Hubbard, S.S., Birkholzer,

J.T., 2013. Effect of dissolved CO_2 on a shallow ground-water system: a controlled release field experiment. Environ. Sci. Technol. 47 (1), 298–305.
Walton, N.R.G., 1989. Electrical conductivity and total dissolved solids – what is their precise relationship? Desalination 72, 275–292.
Waxman, M.H., Smits, L.J.M., 1968. Electrical conductivities in oil-bearing shaly sands. SPE J. 8 (2), 107–122, SPE-1863-PA. http://dx.doi.org/10.2118/1863-PA.
Wilkinson, P.B., Meldrum, P.I., Chambers, J.E., Kuras, O., Ogilvy, R.D., 2006. Improved strategies for the automatic selection of optimized sets of electrical resistivity tomography measurement configurations. Geophysical J. Int. 167, 1119–1126.
Yang, X., Chen, X., Carrigan, C.R., Ramirez, A.L., 2014. Uncertainty quantification of CO_2 saturation estimated from electrical resistivity tomography data at the Cranfield site. Int. J. Greenhouse Gas Control (Submitted for publication).
Zhou, B., Greenhalph, S.A., 2000. Cross-hole resistivity tomography using different electrode configurations. Geophys. Prospect. 48, 887–912.
Zhou, X., Lakkaraju, V.R., Apple, M., Dobeck, L.M., Gullickson, K., Shaw, J.A., Cunningham, A.B., Wielopolki, L., Spangler, L.H., 2012. Experimental observation of signature changes in bulk soil electrical conductivity in response to engineered surface CO_2 leakage. Int. J. Greenh. Gas Control 7, 20–29.